RSC Advances

PAPER

View Article Online
View Journal | View Issue

Cite this: *RSC Adv.*, 2021, **11**, 39493

# Novel heterostructure $Cu_2S/Ni_3S_2$ coral-like nanoarrays on Ni foam to enhance hydrogen evolution reaction in alkaline media†

Yizhi Peng and Hanwei He*

Received 11th October 2021
Accepted 29th November 2021

DOI: 10.1039/d1ra07514d

rsc.li/rsc-advances

Exploring efficient alternatives to precious noble metal catalysts is a challenge. Here, a new type of non-noble metal $Cu_2S/Ni_3S_2$ heterostructure nanosheet array is fabricated on 3D Ni foam. This electrocatalyst has excellent activity and durability to Hydrogen Evolution Reaction (HER) under alkaline conditions. The synergistic catalysis produced by the $\{\bar{2}10\}$ and (034) crystal planes and the increase in charge transfer and the number of active sites caused by lattice defects greatly improve the electrocatalytic activity of $Ni_3S_2$. In the HER process, the $Cu_2S/Ni_3S_2$ interface increases the formation of S–H bonds, and $Cu_2S$ promotes the transformation during the HER process into S-doped CuO, optimizing the adsorption capacity of S-doped sites for H. Among electrocatalysts made with different feed ratios, $Cu_2S/Ni_3S_2$/NF-3, for HER, only needs an overpotential of 50 mV to deliver a current density of 10 mA cm$^{-2}$. This work provides a promising non-noble metal electrocatalyst for water splitting under alkaline conditions.

## 1. Introduction

$H_2$, with its 142 MJ kg$^{-1}$ energy density and nonpolluting reproducibility, is a sustainable energy source worthy of research.[1] The application of hydrogen energy urgently requires exploring cleaner, cheaper, and more efficient hydrogen production technology.[2] A viable clean hydrogen production technology is water splitting, but the overpotential requirements of the hydrogen evolution reaction (HER) and the oxygen evolution reaction (OER) limit the wide application. The slow HER kinetic process enormously limits the overall efficiency.[3] Platinum-based electrocatalysts are recognized as the top electrochemical HER catalysts. However, noble metal catalysts cannot be widely used due to practical factors. Commercially available traditional alkaline electrocatalysts are affordable but not sufficiently active,[4] such as stainless steel,[5] RANEY® nickel,[6] and nickel alloys.[7] Therefore, exploring catalysts that are effective for HER in abundant non-noble metal elements is urgent.

Owing to these practical problems, research has been carried out for decades to find substitutes for noble metals. Among them, high-performance nickel-based materials with excellent electrochemical performance and intrinsic electrocatalytic activity are expected to become the best candidates.[8–11] Among various nickel sulfides, $Ni_3S_2$ with inherent metallic advantages can be a suitable candidate for HER and OER catalysts.[12] As an effective catalyst active ingredient, $Ni_3S_2$ is widely used in electrode materials for supercapacitors and lithium–sulfur batteries.[13] Miaomiao Tong[14] built special 3D $Ni_3S_2$ nanorods@nanosheets, improved their adhesion properties, and exposed more active sites. However, $Ni_3S_2$ can still be modified in terms of increasing conductivity, improving catalytic activity, and exposing active sites.[15,16] Owing to the inevitable sulfur vacancies in $Ni_3S_2$, the regulation of its surface electronic structure has become a way to improve catalytic activity. Metallic element doping is a feasible solution. It can adjust the adsorption/desorption energy, expand the effective surface area, regulate the electronic structure, and exert a synergistic role between ions.[17–19] Relevant literature has reported that Fe,[20] Co,[21] Zn,[22] and Mo[23] doping in $Ni_3S_2$ improves HER or OER performance. However, Cu-doped high-activity $Ni_3S_2$ catalyst with a great HER performance has rarely been reported. Cu, as a doping element, does have a good effect. Several researchers doped Cu as catalytic materials. Zhang *et al.*[24] reported that the charge transfer ability and surface area of Cu-doped Fe–Co oxide have been greatly improved. Co/Cu-modified NiO designed by Guo, ZG *et al.*[25] proved that Cu doping can activate Ni sites at a low overpotential, thereby increasing conductivity and accelerating charge transfer. Until now, studies have focused on the use of doped modified substrate materials. For example, the recent report of Du's group about Cu doped $Ni_3S_2$ has an overpotential of 91 mV.[26] However, the intrinsic catalytic activity of each substance is different, and it is a novel idea to improve the catalytic activity by constructing a heterostructure. There are few reports on the heterostructure of $Cu_2S$ and $Ni_3S_2$, which is a direction worth studying. We used the activity of $Cu_2S$ to construct a heterostructure $Cu_2S/Ni_3S_2$ greatly improved the catalytic activity of $Ni_3S_2$ for hydrogen evolution.

---

*Powder Metallurgy Research Institute, Central South University, Changsha, 410083, China. E-mail: hehanwei@csu.edu.cn*

† Electronic supplementary information (ESI) available. See DOI: 10.1039/d1ra07514d

Based on the above viewpoints, a two-step hydrothermal method was designed to successfully grow $Cu_2S/Ni_3S_2$ with a stable and regular morphology heterostructure on nickel foam. In the first step, the precursor (Cu–Ni layered double hydroxide [LDH]) of the composite structure of nanosheets and nanowires is prepared by changing the feed ratio and reaction conditions. In the second step, a sulfide ion exchange is used to obtain the target sample ($Cu_2S/Ni_3S_2$/NF). The synergistic effect between $Cu_2S$ and $Ni_3S_2$ of heterostructure makes the material obtain excellent HER performance. $Cu_2S/Ni_3S_2$/NF-3 to achieve a current density of 10 mA $cm^{-2}$ only needs an overpotential of 50 mV, which is much lower than the reported Cu doped $Ni_3S_2$ and Ni–S–Cu systems.[26] The number of active sites calculated by the turnover frequency (TOF) is $3.568 \times 10^{-4}$ mol. Moreover, the actual surface area of $Cu_2S/Ni_3S_2$/NF-3 is about 2.2 times that of $Ni_3S_2$/NF. The high electrocatalytic performance of $Cu_2S/Ni_3S_2$/NF is mainly manifested in the following aspects: 1. After vulcanization, the surface of the layer structure is "coral-like," exposing abundant active sites and allowing the active ingredients to be in close contact with the electrolyte. 2. The combination of $Cu_2S$ and $Ni_3S_2$, $Cu_2S$ is converted into S-doped CuO during the HER process, where CuO introduces a defect level near the Fermi level, accelerates charge transfer and improves intrinsic conductivity.[27] 3. The high conductivity of $Ni_3S_2$ provides a fast charge transfer and promotes the electrocatalytic reaction of the catalyst. 4. High-index $\{\bar{2}10\}$ of $Ni_3S_2$ and exposed (034) crystal plane of $Cu_2S$ improve electrocatalytic performance.

## 2. Experimental section

### 2.1 Experimental materials preparation

In this experiment, chemicals include ionized water (>18.25 mΩ $cm^{-1}$, Millipore), and $CuCl_2 \cdot 2H_2O$, $NiCl_2 \cdot 6H_2O$, $CH_4N_2O$, $NH_4F$, $Na_2S$, all purchased from Sinopharm Chemical Reagent Co., Ltd. The nickel foam (NF) used in all experiment were obtained from Kunshan Desco Electronics Co., Ltd. (Suzhou, China) and the density of NF was 350 g $m^{-2}$.

**2.1.1 Fabricating Ni–Cu LDH nanosheet array on NF.** First, $CuCl_2 \cdot 2H_2O$ and $NiCl_2 \cdot 6H_2O$ were dissolved in deionized water(70 mL) at different molar ratios (the specific feed ratio and the corresponding serial number are shown in Table 1), 10 mmol $CH_4N_2O$ and 4 mmol $NH_4F$ were add in above solution. Then the precursor solution, stirred for 10 minutes, was transferred into a 100 mL Teflon-line stainless autoclave. The prepared clean NF (2 × 5 cm) was immersed in it, then reacted at 120 °C for 6 h. After cooling, the obtained Ni–Cu LDH/NF was washed and then placed at 60 °C to dry overnight in a vacuum oven. Fig. 1 shows the schematic diagram of preparation of $Cu_2S/Ni_3S_2$/NF.

Table 1 Different feed ratios and corresponding numbers

| $CuCl_2 \cdot 2H_2O$ | $NiCl_2 \cdot 6H_2O$ | Corresponding Cu–Ni LDH |
|---|---|---|
| 2 mmol | 2 mmol | Cu–Ni LDH/NF-0 |
| 2 mmol | 4 mmol | Cu–Ni LDH/NF-1 |
| 2 mmol | 8 mmol | Cu–Ni LDH/NF-2 |
| 2 mmol | 18 mmol | Cu–Ni LDH/NF-3 |
| 2 mmol | 24 mmol | Cu–Ni LDH/NF-4 |

**2.1.2 Ni–Cu LDH sulfide to $Cu_2S/Ni_3S_2$.** Prepared 0.2mol $L^{-1}$ $Na_2S$ solution and dried NiCu-LDH were put into Teflon-line stainless autoclave. After reacting at 100 °C for 8 h, the black $Cu_2S/Ni_3S_2$/NF was obtained. After the $Cu_2S/Ni_3S_2$/NF is washed and dried, the subsequent characterization and performance can be performed.

### 2.2 Preparation for material characterizations and electrochemical measurements

The X-ray diffraction (XRD) of Ni–Cu LDH and $Cu_2S/Ni_3S_2$ was measured using a PANalytical Empyren equipment at 45 kV and 40 mA with a Cu target. The scanning electron microscopy (SEM) images of Ni–Cu LDH and $Cu_2S/Ni_3S_2$ were from Zeiss Sigma 500. Energy dispersive spectroscopy (EDS) analyses were recorded by FEI Talos 200s. The valence states of the elements on the electrode surface were obtained by an ESCALAB 250Xi X-ray photon spectrometer (XPS). Transmission electron microscopy (TEM), selected area electron diffraction (SAED), high-resolution TEM (HRTEM), and scanning TEM were all obtained by using a JEM2100F microscope.

All electrochemical tests use CHI660B electrochemical workstation. A three-electrode system consisting of graphite, saturated calomel electrodes (SCE, KCl saturated) and the sample to be tested was made up in 1 M KOH at 25 °C. The potentials measured in the experiment has been calibrated, and the potential (*vs.* SCE) was converted into a reversible hydrogen electrode (RHE) through the Nernst equation:[28] $E_{vs.\,\mathrm{RHE}} = E_{vs.\,\mathrm{SCE}} + 0.242\ \mathrm{V} + 0.059\ \mathrm{pH}$. The polarization curves were corrected by the equation:[29] $E_{\mathrm{corrected}} = E_{vs.\,\mathrm{RHE}} - iR$ linear sweep voltammetry (LSV), cyclic voltammetry (CV), electrochemical impedance spectroscopy (EIS) and continuous CV cycles were used to evaluate the electrocatalytic performance of the catalyst.

## 3. Experimental results

### 3.1 $Cu_2S/Ni_3S_2$ structure analysis

NF with 3D conductive network structure and macropores was used as a base material for electrocatalyst growth. After the two-step hydrothermal reaction mentioned above, the silver white

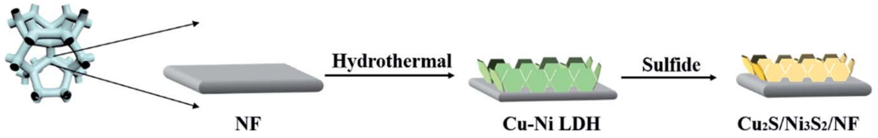

Fig. 1 Schematic diagram of preparation of $Cu_2S/Ni_3S_2$/NF.

NF changed to brick red (the NiCu LDH precursor) and then black ($Cu_2S/Ni_3S_2/NF$). The SEM images in Fig. 2(a)–(f) can visually present the microscopic morphology of the sample. Fig. 2(a)–(c) show the SEM images of NiCu LDH. NiCu LDH is uniformly anchored on the NF substrate in a sheet-like manner. After further increasing the magnification, "nano fluff" was evenly distributed on the nanosheets. Compared with NiCu LDH, the SEM images of $Cu_2S/Ni_3S_2/NF$ did not change significantly, as shown Fig. 3(d)–(f), indicating that the required LDH layered structure can exist stably. After vulcanization, the "nano fluff" is transformed into a "coral" with a rough surface, exposing more active sites. The SEM picture of $Cu_2S/Ni_3S_2/NF$ after 58 h chronopotentiometry test is placed in the support information. As shown in Fig. S1,† some cracks appeared on $Cu_2S/Ni_3S_2$ layer after the test. And the original thin nanosheets are transformed into a stacked coral layer. This transition from "nano fluff" to "rough coral" increases the specific surface area and helps improve electrocatalytic activity.

Furthermore, Fig. 2(g) shows the XRD pattern of $Ni_3S_2/NF$ and $Cu_2S/Ni_3S_2/NF$. Both XRD spectra have the same three strong peaks, based foam nickel (PDF #70-1849). The diffraction peaks of both at $2\theta = 21.75°$, $31.10°$, $37.78°$, $49.73°$, and $55.16°$ correspond to $Ni_3S_2$ (PDF #44-1418) (101), (110), (003), (113), and (122) crystal planes, respectively. Obviously, the characteristic peak of $Cu_2S$ (PDF #33-0490) appeared in the XRD spectrum (indicated by the orange line) after Cu was added. The XRD spectrum qualitatively showed the existence of $Cu_2S/Ni_3S_2$. EDS confirms that Ni, Cu, and S are present in $Cu_2S/Ni_3S_2/NF$ sample, and their atomic ratio is close to the feed ratio. The $Cu_2S/Ni_3S_2/NF$ after 58 h chronopotentiometry test was characterized by XRD. As shown in the ESI Fig. S2,† after the 58 h stability test, the XRD spectrum of $Cu_2S/Ni_3S_2/NF$ showed a CuO

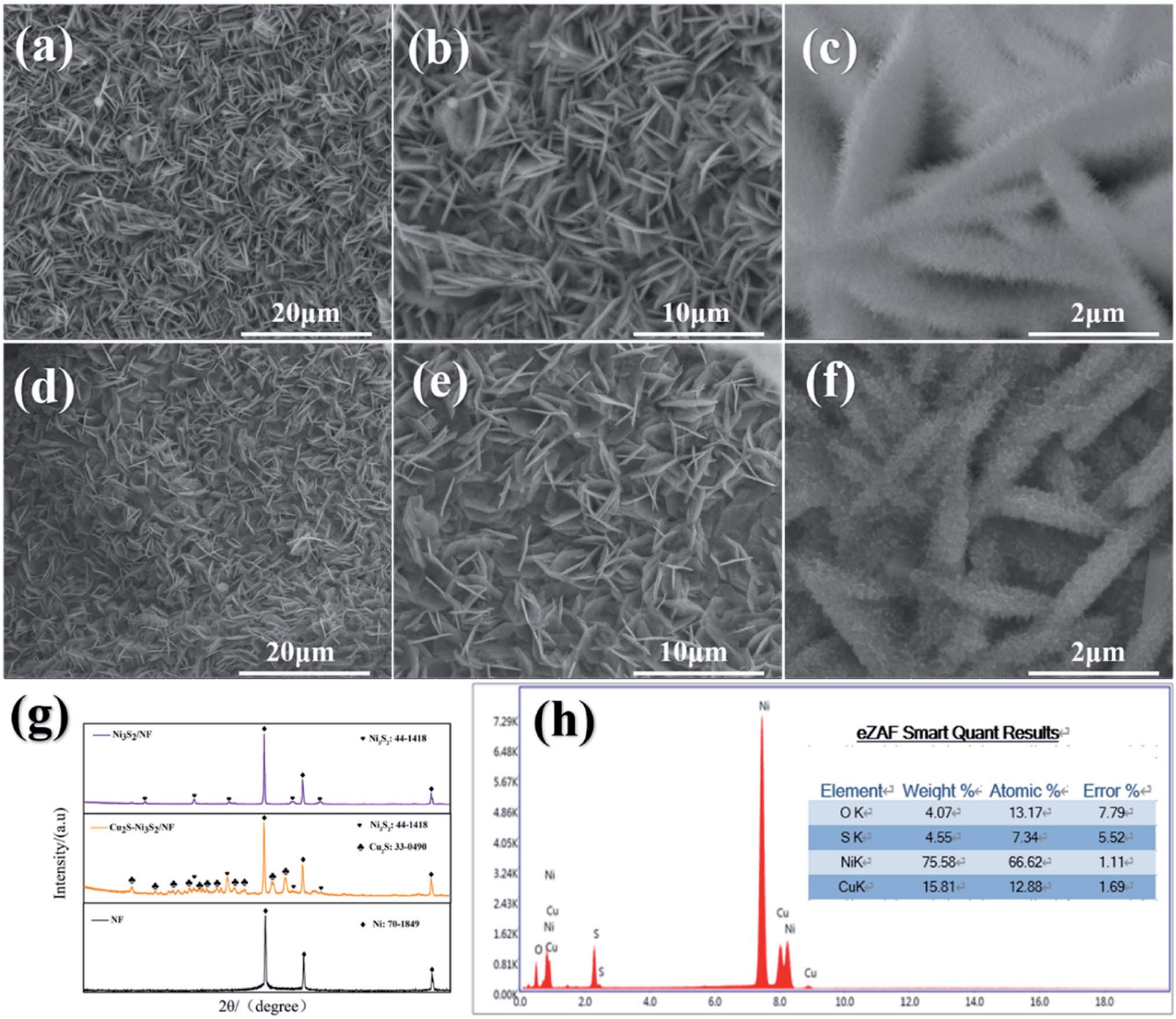

eZAF Smart Quant Results

| Element | Weight % | Atomic % | Error % |
|---|---|---|---|
| O K | 4.07 | 13.17 | 7.79 |
| S K | 4.55 | 7.34 | 5.52 |
| NiK | 75.58 | 66.62 | 1.11 |
| CuK | 15.81 | 12.88 | 1.69 |

Fig. 2 (a–c) SEM image of NiCu LDH-3, (d–f) SEM image of $Cu_2S/Ni_3S_2/NF$-3, (g) XRD pattern of $Ni_3S_2/NF$, $Cu_2S/Ni_3S_2/NF$ and NF, (h) EDS image of $Cu_2S/Ni_3S_2/NF$.

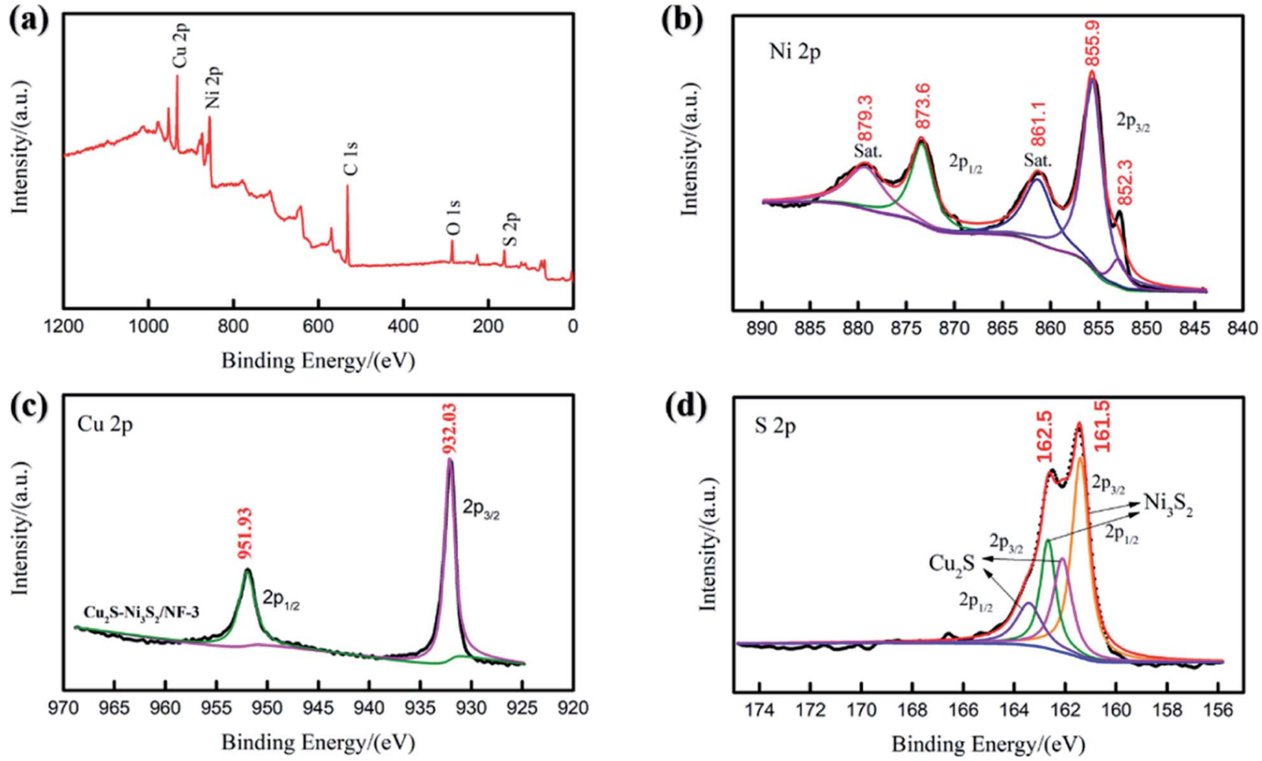

Fig. 3 (a) XPS survey spectrum for $Cu_2S/Ni_3S_2$. XPS spectra of $Cu_2S/Ni_3S_2$ in the (b) Ni 2p, (c) Cu 2p and (d) S 2p regions.

peak (PDF #89-5899) that had not appeared before the test. The diffraction peaks at $2\theta = 35.6°$, $38.8°$, and $48.7°$ correspond to CuO ($-111$), (111), and ($-202$) crystal planes, respectively. The intensity of the $Cu_2S$ peak weakened, indicating that $Cu_2S$ was partially converted to CuO.

In addition, the element composition of $Cu_2S/Ni_3S_2$/NF-3 can be obtained by XPS. The overall XPS spectrum of $Cu_2S/Ni_3S_2$/NF-3 is shown in Fig. 3(a), where Ni, Cu, and S are present. Fig. 3(b) shows the XPS spectrum of the Ni 2p region, where the intensities of the Ni $2p_{1/2}$ and Ni $2p_{3/2}$ peaks are 855.48 eV and 873.23 eV, respectively, indicating that Ni exists in the form of $Ni_3S_2$.[30] The peaks of 879.2 and 860.8 eV are the concomitant satellites.[31,32] The small peak on the far right (852.8 eV) is a typical metal nickel sulfide or metal nickel peak.[33] In the XPS spectrum of Cu 2p region shown in Fig. 3(c), 932.03 eV is the peak of Cu $2p_{3/2}$ in $Cu_2S$, and 951.93 eV is the peak of Cu $2p_{1/2}$.[34] The last picture in Fig. 3(d) is the XPS spectrum of S 2p, where 162.48 and 161.48 eV are attributed to S $2p_{1/2}$ and $2p_{3/2}$ in $Ni_3S_2$, respectively.[35] And 162.25 eV is attributed to S $2p_{3/2}$ in $Cu_2S$. All XPS spectra fully prove that the synthesized sample is $Cu_2S/Ni_3S_2$. After 58 h chronopotentiometry test, the XPS spectra of the electrode is placed in the ESI Fig. S3.† In Fig. S3(b)† shows that Ni $2p_{3/2}$ and Ni $2p_{1/2}$ of $Ni_3S_2$ are the main strong peaks, which can match the conclusion of XRD (Fig. S2†). Moreover, in Fig. S3(b).† The Cu 2p spectra (Fig. S3(c)†) shows $Cu^+$ and $Cu^{2+}$ peaks. Among them, the Cu $2p_{3/2}$ and Cu $2p_{1/2}$ match with the $Cu_2S$ and the strong $Cu^{2+}$ satellite match with the CuO detected by XRD (Fig. S2†). Compared with the original XPS spectra, the intensity of S 2p (Fig. S3(d)†) is reduced after the chronopotentiometry test. We suspected that the heterostructure $Cu_2S/Ni_3S_2$ catalyst is converted to sulfur-doped CuO in this process. It is reported that the $\Delta G_{H^*}$ of sulfur-doped CuO is lower than that of pure CuO.[36] The heterostructure between $Cu_2S/Ni_3S_2$ promotes interface electron transfer. The Ni sites at the $Cu_2S/Ni_3S_2$ interface interact with O in water molecules to adsorb water molecules on the surface. After that, the water molecules adsorbed on the Ni site interact with hydrogen bonds or form S–H bonds, which accelerate the adsorption and dissociation of water and increase the speed of the Volmer step.[37–39] It is reported that S optimizes the free energy of H* (ΔEH*) adsorption of CuO, and the O site of CuO near the S-doped site increased the H adsorption capacity.[40]

Fig. 4(a) clearly shows the TEM image of $Cu_2S/Ni_3S_2$/NF layer structure stacked on top of one another. The SAED pattern of $Cu_2S/Ni_3S_2$/NF in Fig. 4(b) shows typical polycrystalline diffraction rings. These calibrated diffraction rings can correspond well to the peak of the XRD spectrum. Comparing with the PDF card confirmed it to be $Ni_3S_2$. The diffraction ring of the (034) crystal planes of $Cu_2S$ can also be observed, which corresponds to the strong peak appearing after Cu doping in the XRD spectrum. The exposed (034) crystal planes of $Cu_2S$ is beneficial for the improvement of the HER performance of the catalyst. The HRTEM lattice fringe image of $Cu_2S/Ni_3S_2$ is in Fig. 4(c). The crystal planes with interplanar spacings of 0.287, 0.234, and 0.237 nm correspond to the (110), (021), and (003) crystal planes of $Ni_3S_2$ (PDF#44-1418), respectively. The exposed crystal surface of the catalyst has an important influence on its catalytic performance. The angle between the two (110) is 60°, indicating that the thermodynamically stable {001} crystal planes is exposed. The angle between (003) and (021) is about 70.5°, then

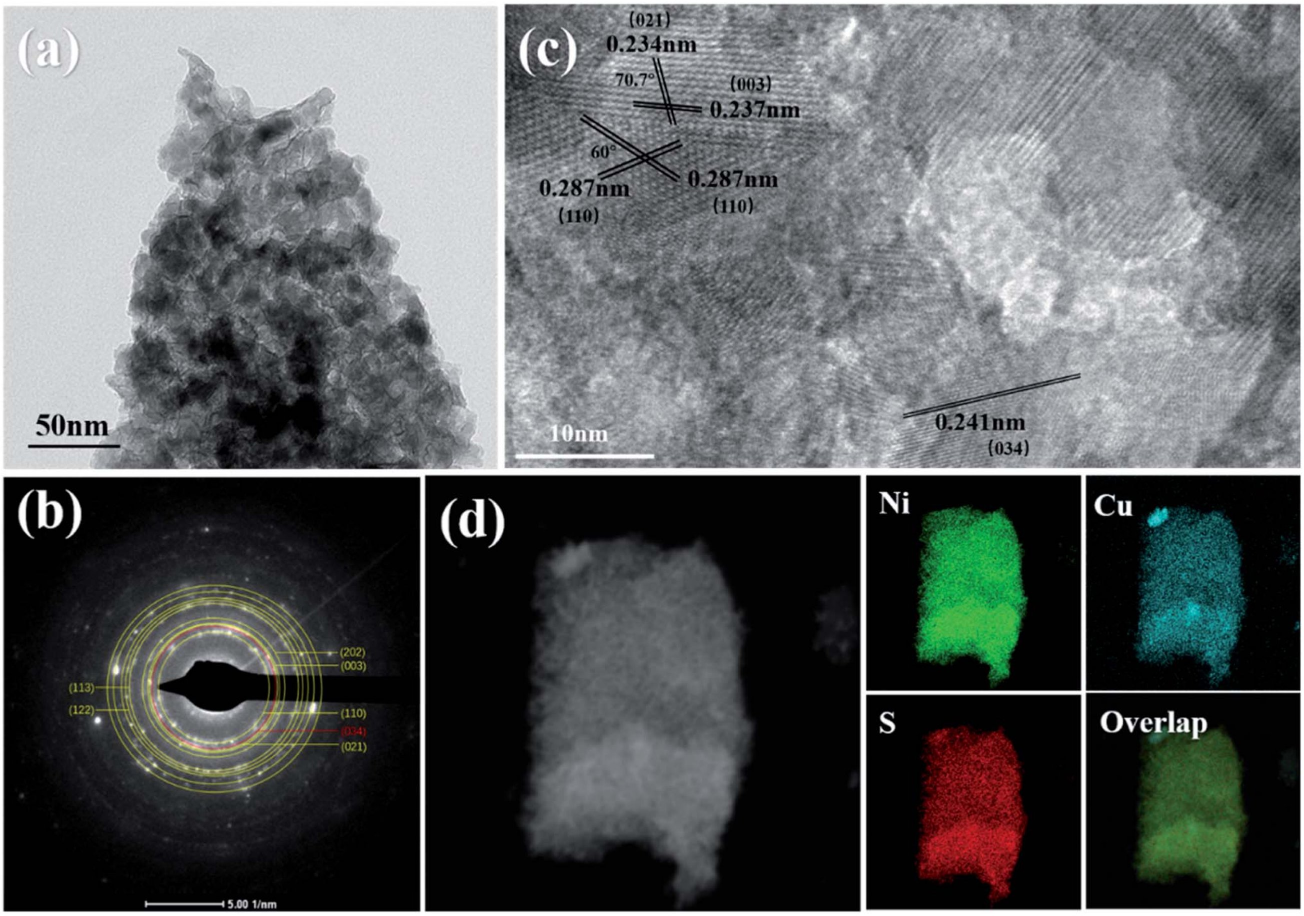

Fig. 4 (a) TEM image of $Cu_2S/Ni_3S_2$ layer structure, (b) SAED pattern and (c) HRTEM image of $Cu_2S/Ni_3S_2$, (d) mapping of Ni, Cu, S and overlap images of $Cu_2S/Ni_3S_2$ nanosheet.

high-index $\{\bar{2}10\}$ is exposed.[41] Research by Liang-Liang Feng *et al.*[41] showed that the synergistic catalysis produced by the nanosheet array and the exposed $\{\bar{2}10\}$ high-index facets help improve electrocatalytic performance. Numerous disordered defects and the exposed (034) crystal planes of $Cu_2S$ can also be observed in the HRTEM image, indicating that the exposed active sites and electrical conductivity can be increased.[42] Moreover, the mapping of $Cu_2S/Ni_3S_2$ nanosheet in Fig. 4(d) reflects that Ni, S, and Cu are evenly distributed on the nanosheets, which is conducive to the uniform dispersion of active sites.

Table 2 Comparison of overpotential of different samples

| Catalysts | Current density ($j$ mA cm$^{-2}$) | Overpotential ($\eta$/mV) |
|---|---|---|
| Pt/C | 10 | 31 |
| $Ni_3S_2$/NF | 10 | 180 |
| $Cu_2S/Ni_3S_2$/NF-0 | 10 | 182 |
| $Cu_2S/Ni_3S_2$/NF-1 | 10 | 159 |
| $Cu_2S/Ni_3S_2$/NF-2 | 10 | 122 |
| $Cu_2S/Ni_3S_2$/NF-3 | 10 | 50 |
| $Cu_2S/Ni_3S_2$/NF-4 | 10 | 134 |

### 3.2 Catalyst electrochemical performance analysis

**3.2.1 Catalyst HER performance.** The LSV of Pt/C, $Ni_3S_2$/NF, and $Cu_2S/Ni_3S_2$/NF-$x$ ($x$ represents various feed ratios) was

Table 3 Comparison of the electrocatalysts performance of $Cu_2S/Ni_3S_2$/NF and other $Ni_3S_2$

| Catalysts | Electrolyte Solution | Overpotential ($\eta_{10}$) |
|---|---|---|
| $Cu_2S/Ni_3S_2$/NF-3 | 1 M KOH | 50 mV |
| S-v-$Ni_3S_2-xP_{x-4}$ (ref. 44) | 1 M KOH | 89 mV |
| Mo-doped $Ni_3S_2$ (ref. 45) | 1 M KOH | 90 mV |
| V-doped $Ni_3S_2$/NiS[46] | 1 M KOH | 85 mV |
| $CoNi_2S_4/Ni_3S_2$@NF[47] | 1 M KOH | 171 mV |

Table 4 Number of active sites of $Cu_2S/Ni_3S_2$/NF-$x$ and $Ni_3S_2$/NF

| Catalysts | Number of active sites ($\times 10^{-4}$ mol) |
|---|---|
| $Ni_3S_2$/NF | 1.625 |
| $Cu_2S/Ni_3S_2$/NF-2 | 2.639 |
| $Cu_2S/Ni_3S_2$/NF-3 | 3.568 |
| $Cu_2S/Ni_3S_2$/NF-4 | 3.533 |

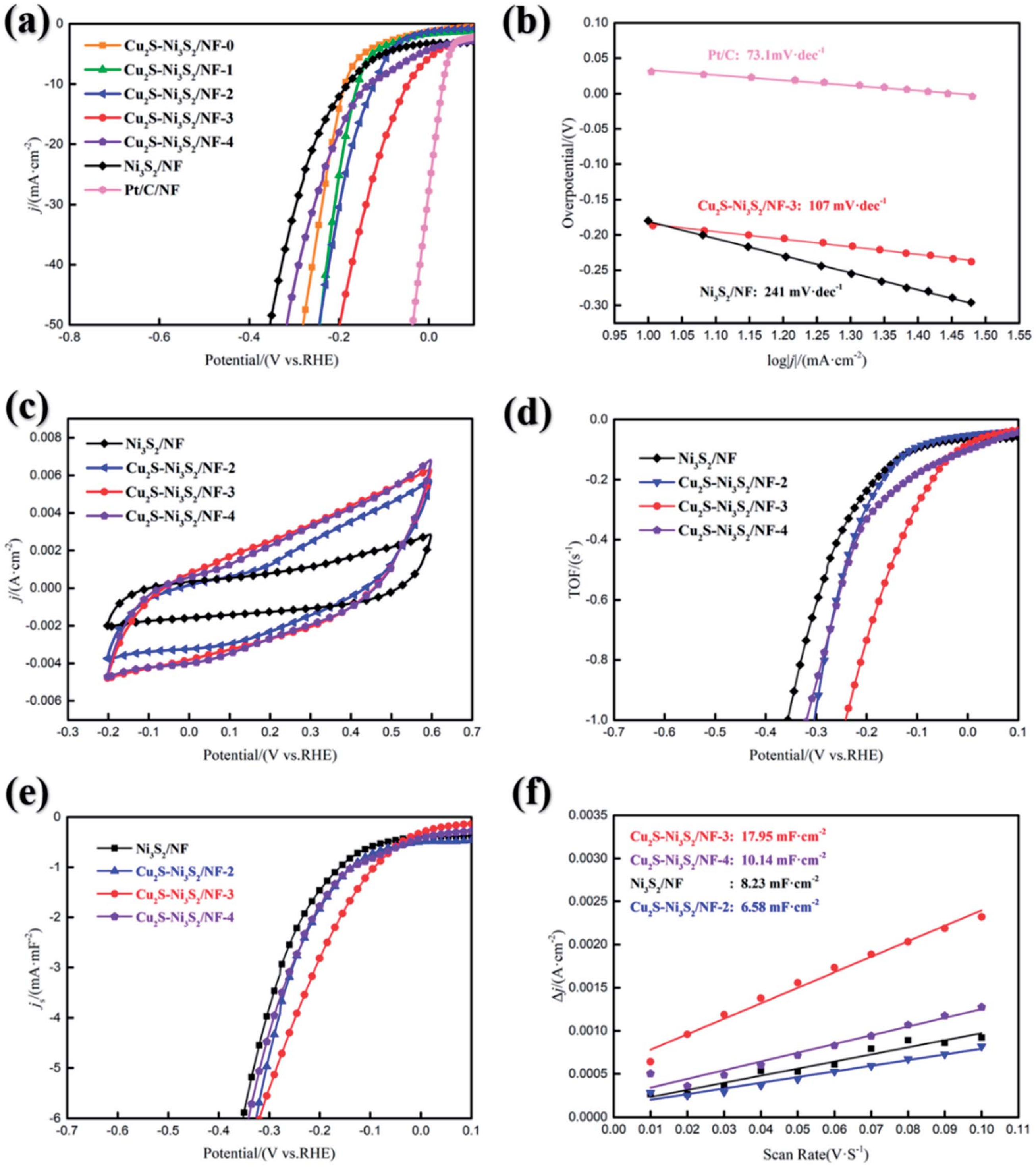

Fig. 5 (a) *iR*-Corrected linear sweep voltammetry curves of $Ni_3S_2$/NF and $Cu_2S/Ni_3S_2$/NF-*x* (*x* represents various feed ratios) for HER in 1 M KOH at 5 mV s$^{-1}$, (b) Tafel plots of $Ni_3S_2$/NF, Pt/C and $Cu_2S/Ni_3S_2$/NF-3, (c) CVs of $Ni_3S_2$/NF and $Cu_2S/Ni_3S_2$/NF-*x* at pH = 7 at the scan rate of 50 mV s$^{-1}$, (d) TOF curves of $Ni_3S_2$/NF and $Cu_2S/Ni_3S_2$/NF-*x*, (e) polarization curves of $Ni_3S_2$/NF and $Cu_2S/Ni_3S_2$/NF-*x* normalized by the ECSA, (f) measured capacitive currents plotted as a function of scan rate.

evaluated in 1 M KOH solution. Comparing the polarization curves clearly shows that Pt/C has the best HER performance ($\eta_{10} = 31$ mV), whereas $Ni_3S_2$/NF requires 180 mV. The $Cu_2S/Ni_3S_2$/NF-3 curve, which is closest to Pt/C curve, requires an overpotential of 50 mV at 10 mA cm$^{-2}$. The overpotentials of five samples are shown in Table 2. Compared with $Ni_3S_2$/NF, the HER performance of $Cu_2S/Ni_3S_2$/NF is indeed improved much. However, experiments have shown that the amount of Cu

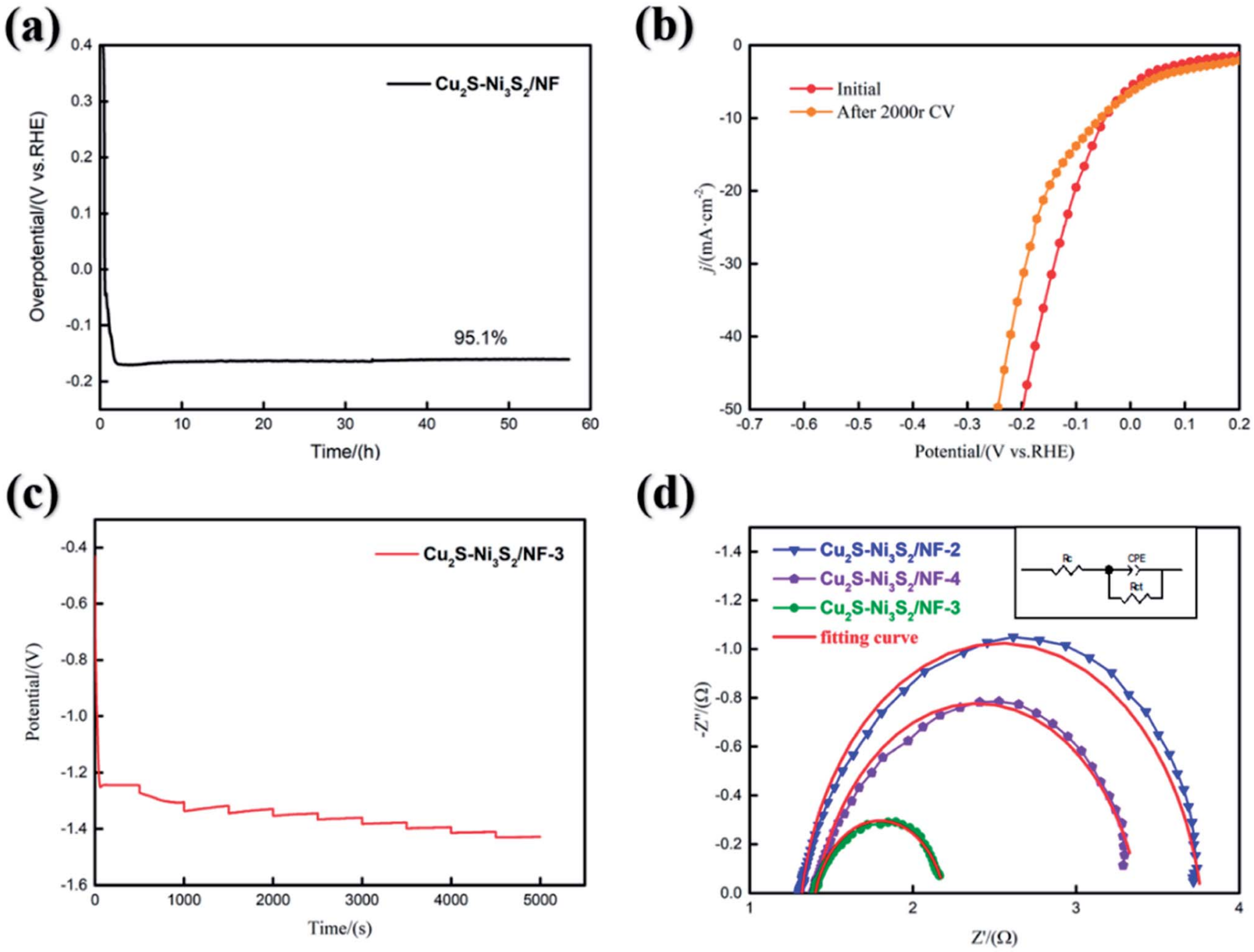

Fig. 6 (a) The chronopotentiometry curve of $Cu_2S/Ni_3S_2/NF$ at constant current density of 10 mA $cm^{-2}$. (b) The polarization curves of $Cu_2S/Ni_3S_2/NF$-3 before and after 2000 CV cycles. (c) Stability test of $Cu_2S/Ni_3S_2/NF$-3 carried out at multiple currents. (d) Impedance Nyquist plots of $Cu_2S/Ni_3S_2/NF$-2, $Cu_2S/Ni_3S_2/NF$-3 and $Cu_2S/Ni_3S_2/NF$-4.

cannot be too much, which is consistent with Byung Keun Kim's report[43] that excessive Cu will increase the internal stress and cause the coating to fall off, thereby reducing catalytic performance. $Cu_2S/Ni_3S_2/NF$ was also compared with the results of other scientific researchers. Detailed data can be found in Table 3.

In alkaline solution, HER follows Volmer–Tafel or Volmer–Heyrovsky mechanism.[48] They all consist of three steps: 1. Discharge ($H_2O + e^- \rightarrow H^* + OH^-$, Volmer reaction) 2. Electrochemical desorption ($H_2O + H^* + e^- \rightarrow H_2 + OH^-$, Heyrovsky reaction) and 3. Recombination ($2H^* \rightarrow H_2$, Tafel reaction). The calculated Tafel slope of $Cu_2S/Ni_3S_2/NF$-3 is 107 mV $dec^{-1}$ (lower than 120 mV $dec^{-1}$), indicating that hydrogen evolution is mainly limited by the Volmer reaction and follows the Volmer–Heyrovsky mechanism. The Tafel slope of $Cu_2S/Ni_3S_2/NF$-3 is clearly much smaller than that of $Ni_3S_2/NF$, indicating that $Cu_2S/Ni_3S_2/NF$-3 catalytic reaction kinetics is faster in an alkaline medium, and the catalytic activity of HER is better.[49]

Turnover frequency (TOF) can be used to reflect intrinsic activity.[50] First, CV curves were measured in a ph = 7 phosphate buffer saline solution at a scan rate of 50 mV $s^{-1}$ and a voltage range of −0.2–0.6 V. Then, the number of active sites was calculated from the method reported by Merki.[51] In Table 4, the active sites loaded on the $Cu_2S/Ni_3S_2/NF$-3 surface is $3.568 \times 10^{-4}$ mol, which is more than $Ni_3S_2/NF$ ($1.625 \times 10^{-4}$ mol). This result may be related to the coral-like surface on the nanosheet shown in the SEM image. This specific morphology can expose more active sites. The calculated TOFs are shown in Fig. 5(d). The overpotentials of $Ni_3S_2/NF$, $Cu_2S/Ni_3S_2/NF$-2∼4 at TOF of 0.2 $S^{-1}$ are 182, 168, 72, and 119 mV, respectively. In Fig. 6(a), TOFs denote that $Cu_2S/Ni_3S_2/NF$-3 has a higher catalytic activity.

Electrochemical Active Surface Area (ECSA) test was carried out. First, the CV curves were measured at various scan rate. Then, Half of the values of the positive and negative current density differences ($\Delta j$) at the median value of the scanning range are plotted *versus* the CV scanning rates in Fig. 5(f). The electrochemical double layer charge ($C_{dl}$) value can be obtained from the fit slope. $Cu_2S/Ni_3S_2/NF$-3 and $Ni_3S_2/NF$ are both cut into 1 cm × 1 cm rectangles, with the same geometric surface area. The $C_{dl}$ of $Cu_2S/Ni_3S_2/NF$-3 (17.95 mF $cm^{-2}$) is approximately 2.2 times that of $Ni_3S_2$/NF (8.23 mF $cm^{-2}$), indicating that the actual surface area of $Cu_2S/Ni_3S_2$/NF-3 is larger. From Fig. S4,† the surface loading of $Cu_2S/Ni_3S_2$ is 2.8 mg $cm^{-2}$.

The chronopotentiometry curve was measured to evaluate the mechanical strength and excellent mass transfer performance of $Cu_2S/Ni_3S_2$/NF-3. In Fig. 6(a), $Cu_2S/Ni_3S_2$/NF can maintain 95.1% activity stably for at least 58 hours. The fluctuation of the curve in the first 30 minutes is due to the gradual increase in the potential during the activation phase caused by the removal of the hydroxide/oxide on the electrode surface.[52] A CV was performed 2000 times continuously from 100 mV to −300 mV. In Fig. 6(b), the HER performance of $Cu_2S/Ni_3S_2$/NF-3 decreased slightly after the CV and need 70 mV to 10 mA $cm^{-2}$. Multistep chronopotentiometry (from 10 mA to 100 mA with 10 mA interval) was used to evaluate the mass transfer and stability of $Cu_2S/Ni_3S_2$/NF-3. The electrode reaction kinetics can be studied by EIS. The Nyquist diagrams of $Cu_2S/Ni_3S_2$/NF-2,3,4 were obtained at 200 mV. The equivalent circuit in Fig. 6(d): a constant-phase element (CPE) connected in parallel with a charge transfer resistance ($R_{ct}$), then an electrolyte resistance ($R_s$) is connected in series. The fitting line represented by the red line is semicircular, which means that the charge transfer controls the entire HER. $R_{ct}$ can be determined in the semicircular low-frequency region to reflect the electron transport efficiency.[53] The $R_{ct}$ values of $Cu_2S/Ni_3S_2$/NF-2,3,4 are 2.44 Ω, 0.79 Ω, and 1.98 Ω, respectively. $Cu_2S/Ni_3S_2$/NF-3 has the smallest $R_{ct}$, which means fast electron transfer. The excellent HER performance of $Cu_2S/Ni_3S_2$/NF-3 also echoes this result. By contrast, a small $R_s$ value indicates that the bonding between the catalyst and the current collector is good.[54] The impedance results of $Cu_2S/Ni_3S_2$/NF-3 are consistent with the previous HER results, which can prove that it can be a candidate with excellent HER kinetics and outstanding electron transport performance.

## 4. Conclusion

Overall, the heterostructure $Cu_2S/Ni_3S_2$ were successfully synthesized by two-step hydrothermal method and exhibited excellent HER activity. Compared with the recently reported system, $Cu_2S/Ni_3S_2$/NF-3 has a lower overpotential ($\eta_{10} = 50$ mV). After vulcanization, the coral-like rough surface exposes more active sites. The heterostructure of $Cu_2S/Ni_3S_2$ exposes specific $\{\bar{2}10\}$ crystal planes as well as a large number of defects and (034) crystal planes, which helps expose more active sites. The structural characterization is consistent with the electrochemical test results. In HER process, $Cu_2S/Ni_3S_2$ interface increase the formation of S–H bonds, optimizing the adsorption capacity of S-doped sites for H. And $Cu_2S$ promotes the transformation of the HER process into S-doped CuO. Therefore, the combination of $Cu_2S$ and $Ni_3S_2$ further increases the catalytic activity.

## Conflicts of interest

The authors declare no conflict of interest.

## Acknowledgements

Authors very thanks for the help from the friends and the authoritative opinion and suggestions from the reviewers.

## References

1 S. Chu, Y. Cui and N. Liu, The path towards sustainable energy, *Nat. Mater.*, 2017, **16**, 16–22, DOI: 10.1038/nmat4834.
2 Z. W. Seh, J. Kibsgaard, C. F. Dickens, I. B. Chorkendorff, J. K. Norskov and T. F. Jaramillo, Combining theory and experiment in electrocatalysis: insights into materials design, *Science*, 2017, **355**, 146, DOI: 10.1126/science.aad4998.
3 L. Peng, J. Shen, X. Zheng, R. Xiang, M. Deng, Z. Mao, Z. Feng, L. Zhang, L. Li and Z. Wei, Rationally design of monometallic NiO-Ni $_3$ $S_2$/NF heteronanosheets as bifunctional electrocatalysts for overall water splitting, *J. Catal.*, 2018, **369**, 345–351, DOI: 10.1016/j.jcat.2018.11.023.
4 K. Zeng and D. Zhang, Recent progress in alkaline water electrolysis for hydrogen production and applications, *Prog. Energy Combust. Sci.*, 2010, **36**, 307–326, DOI: 10.1016/j.pecs.2009.11.002.
5 M. Gong and H. Dai, A mini review of NiFe-based materials as highly active oxygen evolution reaction electrocatalysts, *J. Nano Res.*, 2015, **8**, 23–39, DOI: 10.1007/s12274-014-0591-z.
6 L. B. Lasia, Studies of the Hydrogen Evolution Reaction on Raney Nickel—Molybdenum Electrodes, *J. Appl. Electrochem.*, 2004, **34**, DOI: 10.1023/B:JACH.0000031161.26544.6a.
7 N. Danilovic, R. Subbaraman and D. Strmcnik, Enhancing the Alkaline Hydrogen Evolution Reaction Activity through the Bifunctionality of $Ni(OH)_2$/Metal Catalysts, *Angew. Chem.*, 2012, **124**, 12663–12666, DOI: 10.1002/anie.201204842.
8 C. Yang, M. Y. Gao, Q. B. Zhang, J. R. Zeng, X. T. Li and A. P. Abbott, *In situ* activation of self-supported 3D hierarchically porous Ni3S2 films grown on nanoporous copper as excellent pH-universal electrocatalysts for hydrogen evolution reaction, *Nano Energy*, 2017, **36**, 85–94, DOI: 10.1016/j.nanoen.2017.04.032.
9 X. F. A. B., Y. S. A., J. S. A., L. H. A. and Z. H. B., Superhydrophilic 3D peony flower-like Mo-doped Ni 2 S 3 @NiFe LDH heterostructure electrocatalyst for accelerating water splitting, *Int. J. Hydrogen Energy*, 2021, **46**, 5169–5180, DOI: 10.1016/j.ijhydene.2020.11.018.
10 J. J. Duan, Z. Han, R. L. Zhang, J. J. Feng and A. J. Wang, Iron, manganese co-doped $Ni_3S_2$ nanoflowers *in situ* assembled by ultrathin nanosheets as a robust electrocatalyst for oxygen evolution reaction, *J. Colloid Interface Sci.*, 2020, **588**, DOI: 10.1016/j.jcis.2020.12.062.
11 Q. Ma, C. Hu, K. Liu, S. F. Hung, D. Ou, H. Ming Chen, G. Fu and N. Zheng, Identifying the Electrocatalytic Sites of Nickel Disulfide in Alkaline Hydrogen Evolution Reaction, *Nano Energy*, 2017, **41**, 148–153, DOI: 10.1016/j.nanoen.2017.09.036.

12 Y. J. Liu, C. L. Luan, J. T. Yang, Y. Dong, Y. Wang, C. L. Qin, Z. Dong, S. Q. Wang, X. P. Dai and X. Zhang, In situ fabrication of dynamic self-optimizing $Ni_3S_2$ nanosheets as an efficient catalyst for the oxygen evolution reaction, *DTr*, 2019, **49**, 70–78, DOI: 10.1039/c9dt03885j.

13 M. R. Gao, J. X. Liang, Y. R. Zheng, Y. F. Xu, J. Jiang, Q. Gao, J. Li and S. H. Yu, An efficient molybdenum disulfide/cobalt diselenide hybrid catalyst for electrochemical hydrogen generation, *Nat. Commun.*, 2015, **6**, 5982, DOI: 10.1038/ncomms6982.

14 M. Tong, L. Wang, P. Yu, C. Tian, X. Liu, W. Zhou and H. Fu, $Ni_3S_2$ nanosheets *in situ* epitaxially grown on nanorods as high active and stable homojunction electrocatalyst for hydrogen evolution reaction, *ACS Sustainable Chem. Eng.*, 2017, **6**, 2474–2481, DOI: 10.1021/acssuschemeng.

15 X. Luo, P. Ji, P. Wang, R. Cheng and S. Mu, Interface Engineering of Hierarchical Branched Mo-Doped Ni3S2/NixPy Hollow Heterostructure Nanorods for Efficient Overall Water Splitting, *Adv. Energy Mater.*, 2020, **10**, 1–11, DOI: 10.1002/aenm.201903891.

16 X. Liang, Y. Li, H. Fan, S. Deng and X. Xia, Bifunctional NiFe layered double hydroxide@$Ni_3S_2$ heterostructure as efficient electrocatalyst for overall water splitting, *Nanot*, 2019, **30**, 484001, DOI: 10.1088/1361-6528/ab3ce1.

17 J. Jian, L. Yuan, H. Qi, X. Sun, L. Zhang, H. Li, H. Yuan and S. Feng, Sn-Ni3S2 Ultrathin Nanosheets as Efficient Bifunctional Water Split-ting Catalyst with Large Current Density and Low Overpotential, *ACS Appl. Mater. Interfaces*, 2018, **10**, DOI: 10.1021/acsami.8b14603.

18 Y. Zhang, Y. Liu, M. Ma, X. Ren, Z. Liu, G. Du, A. M. Asiri and X. Sun, A Mn-doped Ni2P nanosheet array: an efficient and durable hydrogen evolution reaction electrocatalyst in alkaline media, *Chem. Commun.*, 2017, **53**, 11048–11051, DOI: 10.1039/c7cc06278h.

19 G. Zhang, Y. S. Feng, W. T. Lu, D. He, C. Y. Wang, Y. K. Li, X. Y. Wang and F. F. Cao, Enhanced Catalysis of Electrochemical Overall Water Splitting in Alkaline Media by Fe Doping in Ni3S2 Nanosheet Arrays, *ACS Catal.*, 2018, **8**, 5431–5441, DOI: 10.1021/acscatal.8b00413.

20 N. Xie, D. D. Ma, X. T. Wu and Q. L. Zhu, Facile construction of self-supported Fe-doped Ni3S2 nanoparticle arrays for the ultralow-overpotential oxygen evolution reaction, *Nanoscale*, 2021, **13**, 1807–1812, DOI: 10.1039/d0nr07262a.

21 M. Wang, M. Zhang, W. Song, W. Zhong, X. Wang, J. Wang, T. Sun and Y. Tang, A highly stable CoMo2S4/Ni3S2 heterojunction electrocatalyst for efficient hydrogen evolution, *Chem. Commun.*, 2021, **57**, 785–788, DOI: 10.1039/d0cc06972h.

22 Q. Liu, L. Xie, Z. Liu, G. Du and X. Sun, A Zn-doped Ni3S2 nanosheet array as a high-performance electrochemical water oxidation catalyst in alkaline solution, *Chem. Commun.*, 2017, **53**, 12446–12449, DOI: 10.1039/c7cc06668f.

23 P. Phonsuksawang, P. Khajondetchairit, K. Ngamchuea, T. Butburee and T. Siritanon, Enhancing performance of NiCo2S4/Ni3S2 supercapacitor electrode by Mn doping, *Electrochim. Acta*, 2020, **368**, 137634, DOI: 10.1016/j.electacta.2020.137634.

24 Q. Zhang, N. Liu and J. Guan, Accelerative oxygen evolution by Cu-doping into Fe-Co oxides, *Sustainable Energy Fuels*, 2020, **4**, 143–148, DOI: 10.1039/c9se00928k.

25 Z. Guo, X. Wang, Y. Gao and Z. Liu, Co/Cu-modified NiO film grown on nickel foam as a highly active and stable electrocatalyst for overall water splitting, *DTr*, 2020, **49**, 1776–1784, DOI: 10.1039/c9dt04771a.

26 X. Du, Y. Ding and X. Zhang, Cu-doped Ni3S2 interlaced nanosheet arrays as high-efficiency electrocatalyst boosting the alkaline hydrogen evolution, *ChemCatChem*, 2021, 1824–1833, DOI: 10.1002/cctc.202001838.

27 S. Chu, W. Chen, G. Chen, J. Huang, R. Zhang, C. Song, X. Wang, C. Li and K. Ostrikov, Holey Ni-Cu phosphide nanosheets as a highly efficient and stable electrocatalyst for hydrogen evolution, *Appl. Catal., B*, 2018, **243**, 537–545, DOI: 10.1016/j.apcatb.2018.10.063.

28 Y. Jiao, W. Hong, P. Li, L. Wang and G. Chen, Metal-Organic Framework Derived Ni/NiO Micro-particles with Subtle Lattice Distortions for High-performance Electrocatalyst and Supercapacitor, *Appl. Catal., B*, 2018, **244**, 732–739, DOI: 10.1016/j.apcatb.2018.11.035.

29 A. P. Murthy, J. Theerthagiri, K. Premnath, J. Madhavan and K. Murugan, Single-Step Electrodeposited Molybdenum Incorporated Nickel Sulfide Thin Films from Low-Cost Precursors as Highly Efficient Hydrogen Evolution Electrocatalysts in Acid Medium, *J. Phys. Chem. A*, 2017, **121**, 11108–11116, DOI: 10.1021/acs.jpcc.7b02088.

30 X. B. Wang, J. J. Hu, W. D. Liu, G. Y. Wang, J. An and J. S. Lian, Ni–Zn binary system hydroxide, oxide and sulfide materials: synthesis and high supercapacitor performance, *J. Mater. Chem. A*, 2015, **3**, 23333–23344, DOI: 10.1039/c5ta07169k.

31 Y. Zhu, H. D. Yang, K. Lan, K. Lqbal, Y. Liu, P. Ma, Z. M. Zhao, S. Luo, Y. T. LUO and J. T. Ma, Optimization of iron-doped Ni3S2 nanosheets by disorder engineering for oxygen evolution reaction, *Nanoscale*, 2019, **11**, 2355–2365, DOI: 10.1039/c8nr08469f.

32 A. H. Jayatissa and G. Sumanasekera, Surface and gas sensing properties of nanocrystalline nickel oxide thin films, *Appl. Surf. Sci.*, 2013, **276**, 291–297, DOI: 10.1016/j.apsusc.2013.03.085.

33 M. C. Biesinger, B. P. Payne, L. W. M. Lau, A. Gerson and R. S. C. Smart, X-ray photoelectron spectroscopic chemical state quantification of mixed nickel metal, oxide and hydroxide systems, *Surf. Interface Anal.*, 2009, **41**, 324–332, DOI: 10.1002/sia.3026.

34 X. Xun, H. Liu, Y. Su, J. Zhang, J. Niu, H. Zhao, G. Zhao, Y. Liu and G. Li, One-pot synthesis Ni-Cu sulfide on Ni foam with novel three-dimensional prisms/spheres hierarchical structure for high-performance supercapacitors, *J. Solid State Chem.*, 2019, **275**, 95–102, DOI: 10.1016/j.jssc.2019.04.012.

35 Y. Li, L. Cao, L. Qiao, M. Zhou, Y. Yang, P. Xiao and Y. Zhang, Ni–Co sulfide nanowires on nickel foam with ultrahigh capacitance for asymmetric supercapacitors, *J. Mater. Chem. A.*, 2014, **2**, 6540–6548, DOI: 10.1039/c3ta15373h.

36 Y. G. Lin, Y. K. Hsu, C. J. Chuang, Y. C. Lin and Y. C. Chen, Thermally activated Cu/Cu2S/ZnO nanoarchitectures with surface-plasmon-enhanced Raman scattering, *J. Colloid Interface Sci.*, 2015, **464**, 66–72, DOI: 10.1016/j.jcis.2015.10.043.

37 S. Li, C. Xi, Y. Jin, D. Wu and X. W. Du, Ir-O-V Catalytic Group in Ir-Doped NiV(OH)2 for Overall Water Splitting, *ACS Energy Lett.*, 2019, **4**, 1823–8195, DOI: 10.1021/acsenergylett.9b01252.

38 Y. Liu, Q. Li, R. Si, G. D. Li, W. Li, D. P. Liu, D. Wang, L. Sun, Y. Zhang and X. Zou, Coupling Sub-Nanometric Copper Clusters with Quasi-Amorphous Cobalt Sulfide Yields Efficient and Robust Electrocatalysts for Water Splitting Reaction, *Adv. Mater.*, 2017, **29**, 1606200, DOI: 10.1002/adma.201606200.

39 J. X. Feng, J. Q. Wu, Y. X. Tong and G. R. Li, Correction to Efficient Hydrogen Evolution on Cu Nanodots-Decorated Ni 3 S 2 Nanotubes by Optimizing Atomic Hydrogen Adsorption and Desorption, *J. Am. Chem. Soc.*, 2020, **142**, 18997, DOI: 10.1021/jacs.9b06861.

40 Z. Zang, X. Wang, X. Li, Q. Zhao and Z. Lu, Co 9 S 8 Nanosheet Coupled Cu 2 S Nanorod Heterostructure as Efficient Catalyst for Overall Water Splitting, *ACS Appl. Mater. Interfaces*, 2021, **13**, DOI: 10.1021/acsami.0c20820.

41 L. L. Feng, G. Yu, Y. Wu, G. D. Li, L. Hui, Y. Sun, T. Asefa, W. Chen and X. Zou, High-Index Faceted Ni3S2 Nanosheet Arrays as Highly Active and Ultrastable Electrocatalysts for Water Splitting, *J. Am. Chem. Soc.*, 2015, **137**, 14023–14026, DOI: 10.1021/jacs.5b08186.

42 X. Zhang, Y. Zhao, Y. Zhao, R. Shi, G. Waterhouse and T. Zhang, A Simple Synthetic Strategy toward Defect-Rich Porous Monolayer NiFe-Layered Double Hydroxide Nanosheets for Efficient Electrocatalytic Water Oxidation, *Adv. Energy Mater.*, 2019, **9**, 1–7, DOI: 10.1002/aenm.201900881.

43 K. B. Keun, K. Soo-Kil, C. S. Ki and K. J. Jeong, Enhanced Catalytic Activity of Electrodeposited Ni-Cu-P toward Oxygen Evolution Reaction, *Appl. Catal., B*, 2018, **237**, 409–415, DOI: 10.1016/j.apcatb.2018.05.082.

44 Y. Yang, H. Mao, R. Ning, X. Zhao and W. Cai, Ar Plasma-assisted P-doped Ni3S2 with S Vacancies for efficient electrocatalytic water splitting, *DTr*, 2021, **50**, 2007–2013, DOI: 10.1039/d0dt03711g.

45 H. Xu, Y. Liao, Z. Gao, Y. Qing, Y. Wu and L. Xia, A branch-like Mo-doped Ni3S2 nanoforest as a high-efficiency and durable catalyst for overall urea electrolysis, *J. Mater. Chem. A*, 2021, **9**, 3418–3426, DOI: 10.1039/d0ta09423d.

46 D. Yang, L. Cao, L. Feng, J. Huang and J. Wang, Controlled Synthesis of V-Doped Heterogeneous $Ni_3S_2$/NiS Nanorod Arrays as Efficient Hydrogen Evolution Electrocatalysts, *Langmuir*, 2020, **37**, DOI: 10.1021/acs.langmuir.0c02943.

47 W. J. Dai, K. Ren, Y. A. Zhu, Y. Pan, J. Yu and T. Lu, Flower-like $CoNi_2S_4$/$Ni_3S_2$ nanosheet clusters on nickel foam as bifunctional electrocatalyst for overall water splitting, *J. Alloys Compd.*, 2020, **844**, 156252, DOI: 10.1016/j.jallcom.2020.156252.

48 Y. Wu and H. He, Electrodeposited nickel–iron–carbon–molybdenum film as efficient bifunctional electrocatalyst for overall water splitting in alkaline solution, *Int. J. Hydrogen Energy*, 2018, **44**, 1336–1344, DOI: 10.1016/j.ijhydene.2018.11.168.

49 T. T. Chen, R. Wang, L. K. Li, Z. J. Li and S. Q. Zang, MOF-derived Co9S8/MoS2 embedded in tri-doped carbon hybrids for efficient electrocatalytic hydrogen evolution, *J. Energy Chem.*, 2019, **44**, 90–96, DOI: 10.1016/j.jechem.2019.09.018.

50 R. Nivetha and A. N. Grace, Manganese and zinc ferrite based graphene nanocomposites for electrochemical hydrogen evolution reaction, *J. Alloys Compd.*, 2019, **796**, 185–195, DOI: 10.1016/j.jallcom.2019.05.021.

51 Y. S. Park, W.-S. Choi, M. J. Jang, J. H. Lee, S. Park, H. Jin, M. H. Seo, K.-H. Lee, Y. Yin, Y. Kim, J. Yang and S. M. Choi, Three-Dimensional Dendritic Cu–Co–P Electrode by One-Step Electrodeposition on a Hydrogen Bubble Template for Hydrogen Evolution Reaction, *ACS Sustainable Chem. Eng.*, 2019, **7**, 10734–10741, DOI: 10.1021/acssuschemeng.9b01426.

52 K. Zhang, W. Xiao, J. Li, J. Liu and C. Yan, Two-step Preparation of Porous Nickel-sulfur Electrode for Hydrogen Evolution in Alkaline Water Electrolysis, *Electrochim. Acta*, 2017, **228**, 422–427, DOI: 10.1016/j.electacta.2017.01.105.

53 Y. Niu, X. Qian, C. Xu, H. Liu, W. Wu and L. Hou, Cu-Ni-CoSex quaternary porous nanocubes as enhanced Pt-free electrocatalysts for highly efficient dye-sensitized solar cells and hydrogen evolution in alkaline medium, *Chem. Eng. J.*, 2019, **357**, 11–20, DOI: 10.1016/j.cej.2018.09.116.

54 Y. Tian, J. Yu, H. Zhang, C. Wang, M. Zhang, Z. Lin and J. Wang, 3D porous Ni-Co-P nanosheets on carbon fiber cloth for efficient hydrogen evolution reaction, *Electrochim. Acta*, 2019, **300**, 217–224, DOI: 10.1016/j.electacta.2019.01.101.